JOURNAL OF MATERIALS RESEARCH AND TECHNOLOGY 2022;19:2431–2446

Available online at www.sciencedirect.com

jmr&t Journal of Materials Research and Technology

journal homepage: www.elsevier.com/locate/jmrt

Original Article

Experimental and numerical investigation of laser beam-welded Al–Cu–Li joints using micro-mechanical characteristics

Theano N. Examilioti [a,b,c], *Paraskevas Papanikos* [d], *Nikolai Kashaev* [b], *Benjamin Klusemann* [a,b,*], *Nikolaos D. Alexopoulos* [c]

[a] *Institute of Product and Process Innovation, Leuphana University Lüneburg, D-21335 Lüneburg, Germany*
[b] *Institute of Materials Mechanics, Helmholtz-Zentrum Hereon, D-21502 Geesthacht, Germany*
[c] *Research Unit of Advanced Materials, Department of Financial Engineering, University of the Aegean, 821 32 Chios, Greece*
[d] *Department of Product and Systems Design Engineering, University of the Aegean, 841 00 Syros, Greece*

ARTICLE INFO

Article history:
Received 21 April 2022
Accepted 31 May 2022
Available online 7 June 2022

Keywords:
Al–Cu–Li alloy
Laser beam welds
Local mechanical properties
Microhardness
Microstructure
Finite element model

ABSTRACT

The local tensile mechanical properties of laser beam-welded joints of AA2198 alloy with Al–Si filler wire were experimentally investigated. For this purpose, micro-flat tensile specimens were extracted from the fusion zone and the heat-affected zone. The chemical composition of the filler wire affects the local mechanical properties in the fusion zone, showing an approximately 26% decrease in yield strength from the radiation exposure side to the weld root side. The effect of post–weld heat treatment on the tensile mechanical behavior was additionally investigated for different heat treatment artificial ageing conditions. The maximum yield strength increase was noticed for 48 h of artificial ageing for the weld root side of the fusion zone. Several approximations were proposed to correlate the hardness measurements with the local tensile mechanical properties of the welded joint that allow for a fast assessment of the global tensile mechanical behaviour of the welded joint. To evaluate the effect of (i) artificial ageing and (ii) geometrical imperfections of the weld on the mechanical behavior of the welded joint, finite element analyses were performed, using the local mechanical properties as input to the model. It is shown that the local mechanical properties of the fusion zone play a pivotal role on the strain localization and fracture of the welded joint.

* Corresponding author.
E-mail address: benjamin.klusemann@leuphana.de (B. Klusemann).

https://doi.org/10.1016/j.jmrt.2022.05.197

1. Introduction

Nowadays, aircraft industries are mainly focusing on the efficient design of aircraft structures to achieve weight reduction; this has led to the development of new, innovative light-weight structural materials with high specific mechanical properties as well as good weldability [1]. Aluminum-copper-lithium (Al–Cu–Li) alloys are already established in aerospace structures, mainly due to the high-performance design and weight saving they provide. It is estimated that using these alloys instead of conventional Al–Cu–Mg alloys, one could reduce the structure's weight by approximately 10–15% and increase the stiffness by 20% [2]. The addition of 1 wt.% of lithium (Li), which is the lightest metallic element with a specific weight of 0.534 g/cm^3, can reduce the density of the alloy by 3% and can increase the modulus of elasticity by approximately 6% [3,4]. Third-generation Al–Li alloys such as AA2198, AA2195, AA2050 contain <2 wt.% of Li [5]. This Li concentration is capable to form additional precipitation hardening particles, besides the well-known particles like the S type particles, the δ' (Al_3Li) or δ (AlLi) particles; essential the most important precipitation particles are coming from T_1 (Al_2CuLi) phase [6,7]. The influence of different Cu/Li ratios on the precipitation hardening nucleation and kinetics in such alloying system were analytically reported by Jo and Hirano [8]. Furthermore, the precipitation hardening of Al–Cu–Li alloys is strongly depending on the specific heat-treatment conditions. Several investigations focused on the precipitation and microstructure of Al–Cu–Li alloys under different ageing conditions and the effect on their mechanical properties. For example, Alexopoulos et al. [9] investigated the influence of artificial ageing heat treatment on AA2198 for different ageing holding times at 170 °C. With increasing ageing time, maximum yield strength was observed for 48 h and peak-ageing condition while after 48 h a decrease was noticed, which can be attributed to the over-ageing condition. With increasing ageing temperature, uniform distributed θ' and increased T_1 precipitates, with a small number of δ' particles within the microstructure were reported [10,11].

Next to Al–Li alloys, which are lightweight structural materials, aerospace industries focused on efficient joining techniques such as fusion welding, for a further structural weight reduction as well as for a decrease of the manufacturing costs. Laser beam welding (LBW) is a very popular joining technique that is already established in the aerospace industry for high-strength aluminum alloys, especially for lower fuselage structures [12]. As mentioned by Gialos et al. [13], the exploitation of LBW instead of riveting can provide structural weight savings up to 28% with a respective decrease of the total manufacturing cost by 40%. In this regard, the development of weldable third-generation Al–Li alloys, such as AA2198 offers new possibilities for highly complex applications in aircraft structures by using fusion welding [14].

Several investigations are dealing with the mechanical properties and microstructure of welded Al–Li alloys using filler material [15–17]. In most cases of laser beam-welded (LBWed) joints with Al–Li alloys, filler materials with alloying elements like Si, Cu and Mg, were used to reduce the amount of metallurgical defects, such as hydrogen porosity and hot-cracking, and therefore to achieve high joining efficiency [18,19]. In the case of LBWed AA2060-T8 alloy with AlSi12 filler wire, a joint efficiency of approximately 83% was achieved [16], while only 64% was reached when Al–Mg alloy filler wire was used instead [17]. It was noticed that the exploitation of Al–Mg and Al–Si filler material gives lower joint strength due to the formation of the icosahedral quasi-crystalline phase in the weld of about 63% and 84% of the base material (BM), respectively. Therefore, the Al–Si filler wire seems to be probably the best option to laser beam weld Al–Cu–Li alloys due to the higher joint efficiency and mechanical properties achieved.

In order to study the local mechanical properties of welded joints, several investigations included the exploitation of optical methods like digital image correlation (DIC) [20–22] or even the extraction of extremely small size specimens (often called micro-flat tensile – MFT – specimens) [23–26]. Still, the investigation of the local tensile mechanical properties of LBWed Al–Li alloys using MFT specimens remains very limited due to the complexity of the manufacturing process of the specimens. For example, Zhang et al. [16] investigated the microstructural and local mechanical behavior of LBWed AA2060 alloy with AlSi12 filler wire by using MFT specimens vertical to the weld seam. The local mechanical properties across the joint and in the mid-thickness of the cross-section presented a similar trend as the microhardness measurements. The lowest strength was observed in the fusion zone (FZ), ~225 MPa, with a continuous increase in the heat-affected zone (HAZ), from 330 MPa up to 480 MPa. Dhondt et al. [27] investigated the microstructure heterogeneities and mechanical properties of the weld seam of AA2050 without any filler material. For that reason, the authors have chosen a series of horizontal MFT specimens over the depth of the weld seam. The mechanical properties of the FZ presented no significant variation over depth, with average values approximately 310 MPa for yield strength and around 410 MPa for ultimate tensile strength (UTS), respectively. Additionally, Rao et al. [28] used MFT specimens to determine the local mechanical properties at different positions of the joint. These experimental results from each position were used as an input into a finite element (FE) model to predict the macroscopic behaviour of the complete welded specimens, where simulated and experimental results were in good agreement. Similar, Puydt et al. [29] extracted MFT specimens at various positions of the welded joint which were later used as an input to a FE analysis. It was shown that the geometries of the specimens and of the welding seam play a crucial role in the accuracy of the prediction of the results.

The present study focuses on the local mechanical properties of LBWed joints of AA2198 with Al–Si AA4047 filler wire to investigate the gradient of the mechanical properties inside the weld seam. Additionally, the effect of post welding heat treatment (PWHT) on the local tensile mechanical behavior of the joint was studied. The experimental results were used as input to a FE model to investigate the effect of artificial ageing heat treatment as well as of the possible geometrical imperfections on the local mechanical behavior of the welded samples.

Table 1 – Chemical composition of investigated aluminum alloys (in wt. %).

Alloy	Si	Fe	Cu	Mn	Mg	Li	Zn	Zr	Ag	Ti	Al
AA2198	0.03	0.05	3.35	0.1	0.32	0.99	0.1	0.14	0.27	0.30	Bal.
AA4047	12.0	0.8	0.3	0.15	0.1	–	0.2	–	–	–	Bal.

2. Experimental procedure

The BM used in the present study is the Al–Cu–Li alloy 2198 in T3 temper. The sheets had dimensions of 100 mm (width) × 100 mm (length), with a nominal thickness of 5.0 mm. Aluminum-silicon (Al–Si) 4047 wire, with a diameter of 1.2 mm, was used as filler material for all laser welded joints. The chemical composition of AA2198, which was supplied by Constellium, as well as of the filler material are given in Table 1.

The MFT specimens were machined in the longitudinal (L) direction by electro discharge machining (EDM) with approximately 0.5 mm thickness. The dimensions of the specimens are illustrated in Fig. 1. The MFT specimens were horizontally machined from the BM as well as from the FZ, and from three different positions in depth, top (3.5 mm above weld root side - WRS), middle (2.2 mm above WRS), and bottom (1.0 mm above WRS), while from the BM and HAZ the MFT specimens were extracted vertically to the welding direction, Fig. 2. Preliminary microscopy analysis showed that the width of the FZ for the specific laser process parameters is higher than 2.0 mm and therefore this ensures that the specimens can be extracted from the FZ material, as the width of the MFT specimens is 1.5 mm (Fig. 1). Likewise, preliminary hardness measurements, showed that the HAZ width ranges from 1.0 to 4.0 mm. The vertical MFT specimens had lower thickness (0.5 mm < 3.0 mm) and therefore were safely positioned and machined from the HAZ.

LBW with filler material was performed using an IPG YLS 8000 fibre laser with 8.0 kW of maximum laser power. The characteristics of the used laser system are summarized in Table 2. After a preliminary optimization step, the welding parameters used in the present study were as follows: laser power P_l = 8 kW, welding velocity v = 6.8 m/min, resulting linear heat input HI = 70 J/mm, and wire feed rate v_w = 6.0 mm/min. In all welding processes, Argon was used as shielding gas from the radiation exposure side (RES) and WRS, with a gas flow of 15 1/min and 5.5 1/min, respectively. All surfaces were mechanically milled (0.2 mm layer removed for RES and for WRS) to remove the surface oxidation on the sheet before the welding process. All sheets were LBWed parallel to the rolling direction.

Different artificial ageing heat treatments were performed post to the welding in a Weldotherm PP 270/65 furnace at atmospheric pressure and with ±1 °C temperature control. All sheets were isothermally artificially aged at 170°C for different ageing times, 3 h, 48 h and 98 h, which correspond to under-ageing (UA), peak-ageing (PA) and over-ageing (OA), respectively. The artificial ageing temperature of 170°C as well as the corresponding isothermal ageing times were selected according to the previous study of the authors [30] for comparison purposes.

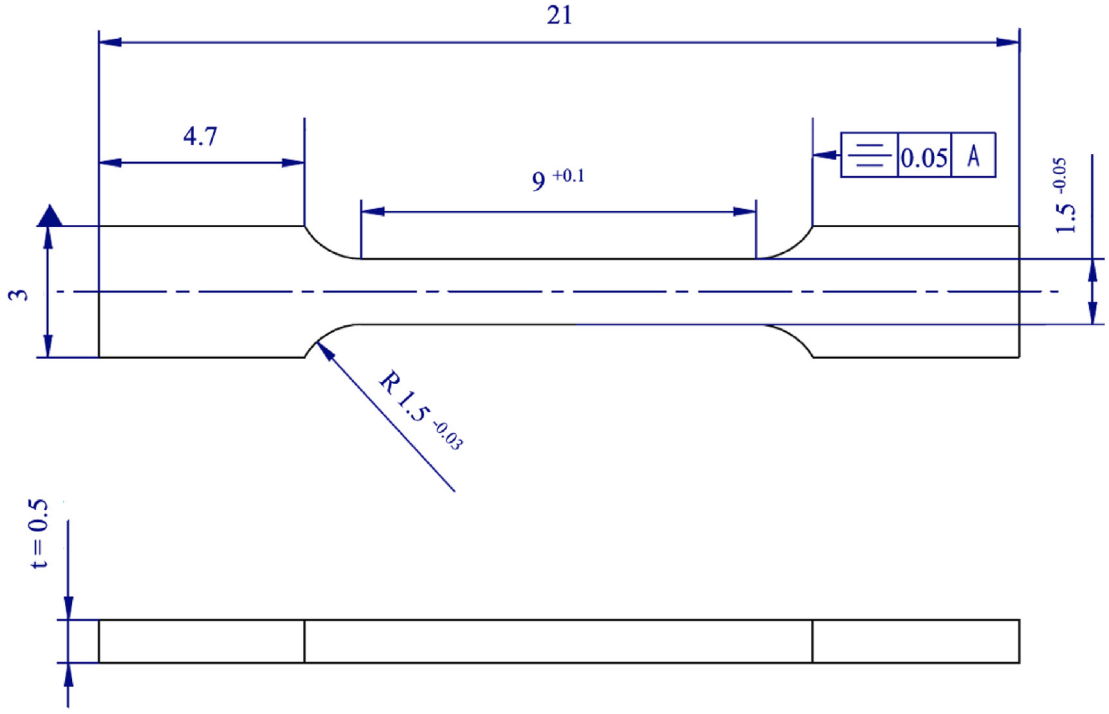

Fig. 1 – Dimensions of micro-flat tensile specimens. All dimensions in mm.

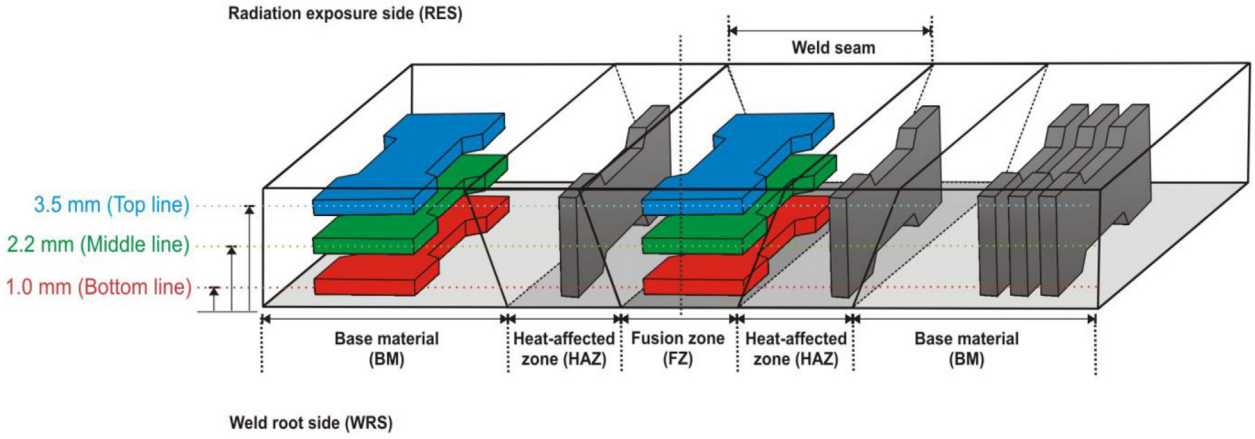

Fig. 2 – Schematic sketch of micro-flat tensile specimens, machined from laser beam-welded AA2198 joints.

The microstructure and the local chemical composition of the welded joints were investigated by using light optical microscopy (LOM) and scanning-electron microscopy (SEM) with energy dispersive X-ray spectroscopy (EDX), respectively. For this purpose, several cross-sections were extracted and investigated from the LBWed joints. The cross-sections were grounded, polished using oxide polishing suspension compound (OP–S) and finally chemically etched by using Keller's reagent to improve the visibility of the microstructure. The characterization of the microstructures was observed with a Leica DMI 5000M microscope equipped with a Leica DFC 450 camera. A more detailed investigation of the microstructure of the welds was performed using Jeol JSM-6490LV SEM. The analysis of the local chemical composition of the FZ was determined by EDX (EDAX Genesis).

Vickers microhardness mapping, according to DIN EN ISO 6507–1:2004 [31], was conducted for all welded joints cross-sections and for all investigated conditions. The semi-automated Vickers microhardness testing device Shimadzu HMV-2000 was used with a test load of 1.96 N and with an indentation time of 15 s. The indentations were set at the specific positions within the BM, HAZ and FZ, with the spacing between the measurements to be 500 μm. The measuring locations are illustrated in Fig. 3a.

The MFT tests were performed on a Zwick testing machine, equipped with ±5.0 kN load-cell. The specimens were tested by exploiting an in-house designed fixture that ensured the correct application of the mechanical load to prevent secondary bending and other unwanted movements of the specimens. All the MFT specimens were tested after PWHT to assess the effect of artificial ageing heat treatment on the respective tensile mechanical properties. In total, more than 50 MFT specimens were tested, including three specimens per each heat treatment condition as well as per different zone of the welded joints. A Fiedler Opto-Electronic (FOE) laser extensometer was used during the tensile tests to measure the deformation of the gauge length of the MFT specimens.

Table 2 – Characteristics of fiber laser used in this study.

Property	Yb fibre laser
Maximum power [kW]	8.0
Focal position [mm]	0.0
Wavelength [μm]	1.07
Beam parameter product [mm × mrad]	7.5
Fibre diameter [μm]	200
Focal length [mm]	300
Collimator length [mm]	120
Laser spot diameter (in focus) [μm]	512
Rayleigh length [mm]	8.784
Irradiance distribution	top-hat

3. Experimental results

3.1. *Microstructural characterization*

The microstructural morphology of a welded joint in the as-welded condition can be seen in Fig. 3. The typical microstructure of LBWed joints of Al–Cu–Li alloys consists of three distinct zones, namely the FZ, the transition zone (TZ) and the HAZ adjacent to the BM. The width of the FZ was measured at different heights, namely, top, middle, and bottom, as presented in Fig. 3b. The TZ is a very narrow zone which can be divided into the partially melted zone (PMZ) and non-dendritic equiaxed grain zone (EQZ), see Fig. 3d. The microstructure of the inner area of the FZ presents equiaxed dendrite grains, Fig. 3c, while the outer area presents columnar grains, Fig. 3d, which is a typical grain structure morphology for welded Al–Li alloys, see e.g., Ning et al. [15] and Zhang et al. [16]. Next to the FZ, the PMZ and EQZ are characterized by spherical and non-dendritic equiaxed grains, respectively. The addition of Li and Zr content plays a significant role in the formation [15,16] and on the width of the EQZ. It has been determined by Gutierrez and Lippold [32] that with an increase of Li and Zr in the filler material, the width of EQZ increases, while with a low concentration of lithium (<0.5 wt.%) and zirconium (~0.03 wt.%) the EQZ does not form. Additionally, it was proposed that the formation mechanism of the EQZ is a consequence of the heterogeneous nucleation of Al_3Zr and $Al_3(Li_x, Zr_{1-x})$ precipitates at the fusion boundary [32,33]. In the present study, EQZ shows to be within the range of approximately 12.5–25 μm and PMZ about 45–50 μm, which are considered as narrow when compared with other Al–Li alloys. The available

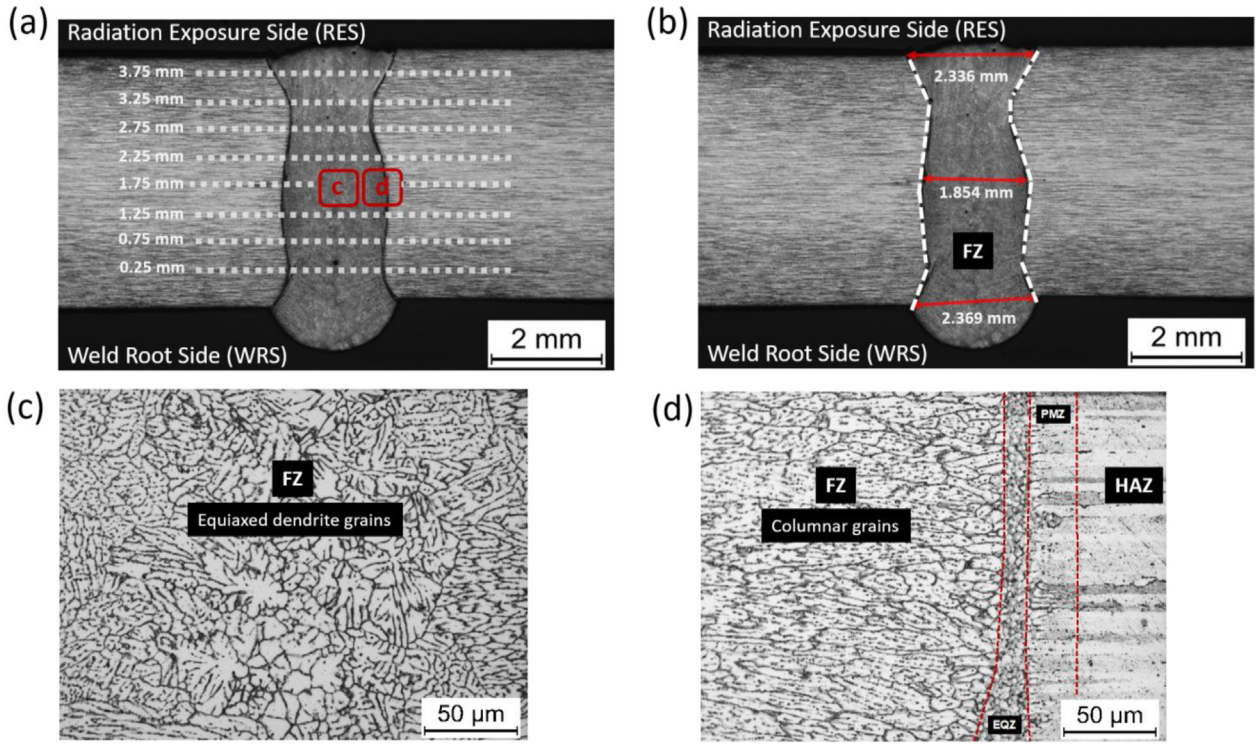

Fig. 3 – Optical micrographs of laser beam-welded AA2198 in the as-welded condition using AA4047 filler wire, showing (a) the example of the location profiles of the mapping for microhardness measurements in the cross-section, (b) the size of the FZ, (c) the dendrite structure of FZ and (d) the EQZ and PMZ at the FZ/HAZ boundary.

results of Zhang et al. [16] for LBWed AA2060-T8 using Al–Si filler material presented a wider EQZ of 40–120 μm. Ning et al. [15] observed also a wider EQZ and PMZ of 25–29 μm and 25–140 μm size, respectively when AA2A97 is welded with AA2319 filler material. Similarly, Zhang et al. [17] determined a wider EQZ of about 30–60 μm for AA2060-T8 using AA5087 filler material.

To study the distribution of the different alloying elements of the filler material in the welded joint, EDX line measurements were performed, as shown in Fig. 4. The first measurement line was over the depth of the FZ, while the second one was in the middle thickness of the cross-section of the welded joint. The EDX lines were measured with a step size of 1.2 μm, including 2.040 points. Fig. 4c shows that the intensity of the Si-signal decreases gradually from RES to WRS. This might be attributed to the non-homogenous dispersion of the Si in the FZ. Si is introduced to the FZ from the filler wire from the RES side. To this end, the high Si content at the RES and the low Si at the WRS can be well explained.

3.2. *Hardness measurements*

Microhardness mapping profiles across the weld cross-section and for different artificial ageing heat treatment conditions are presented in Fig. 5. The 2D hardness map of the as-welded condition shows the lowest hardness being in the middle of the FZ, where a drop of about 29% was noticed, when compared with the HAZ.

In the FZ, a drop in hardness from RES to WRS is noticed, approximately from 105 to 85 $HV_{0.2}$. This can be explained by the gradient concentration of the Al–Si filler material within the FZ. The HAZ consists of an annealed and an over-aged zone with a high hardness of about 111–122 $HV_{0.2}$, Fig. 5a. This high hardness value within the HAZ in the as-welded condition reflects the microstructural changes in this zone, as thermal energy is being given by the adjacent FZ. With increasing artificial ageing up to 3 h (UA condition), the FZ presented a decrease in hardness from RES to WRS of about 42%, Fig. 5b. HAZ presented slightly higher microhardness values of about 118–130 $HV_{0.2}$, when compared with the as-welded condition; the lowest hardness values were noticed in the middle of the cross-section. The highest hardness measurement in the UA condition is noticed in the over-aged zone within the HAZ of about 147 $HV_{0.2}$. Fig. 5c shows that for 48 h ageing time (PA condition), the FZ experienced a drop from RES to WRS of about 30%. Annealed and over-aged zones present again the highest hardness values, approximately 150–170 $HV_{0.2}$. According to Fu et al. [34], this increase in the HAZ was attributed to the presence of precipitation particles and especially the T_1 precipitates during PWHT; their size is increasing with isothermal ageing time up to the PA condition. For 98 h artificially ageing (OA condition), hardness values inside the FZ show a similar drop at PA condition of approximately 31% from RES to WRS, Fig. 5d. A comparable high hardness to PA condition of about 163 $HV_{0.2}$ is observed in the over-aged zone for OA condition. For all investigated PWHTs, the FZ did not present any improvement and is still the weakest zone. Similar results were determined by Kashaev et al. [35] for LBWed AA2198 using Al–Si filler material. Slightly lower microhardness values were obtained at the

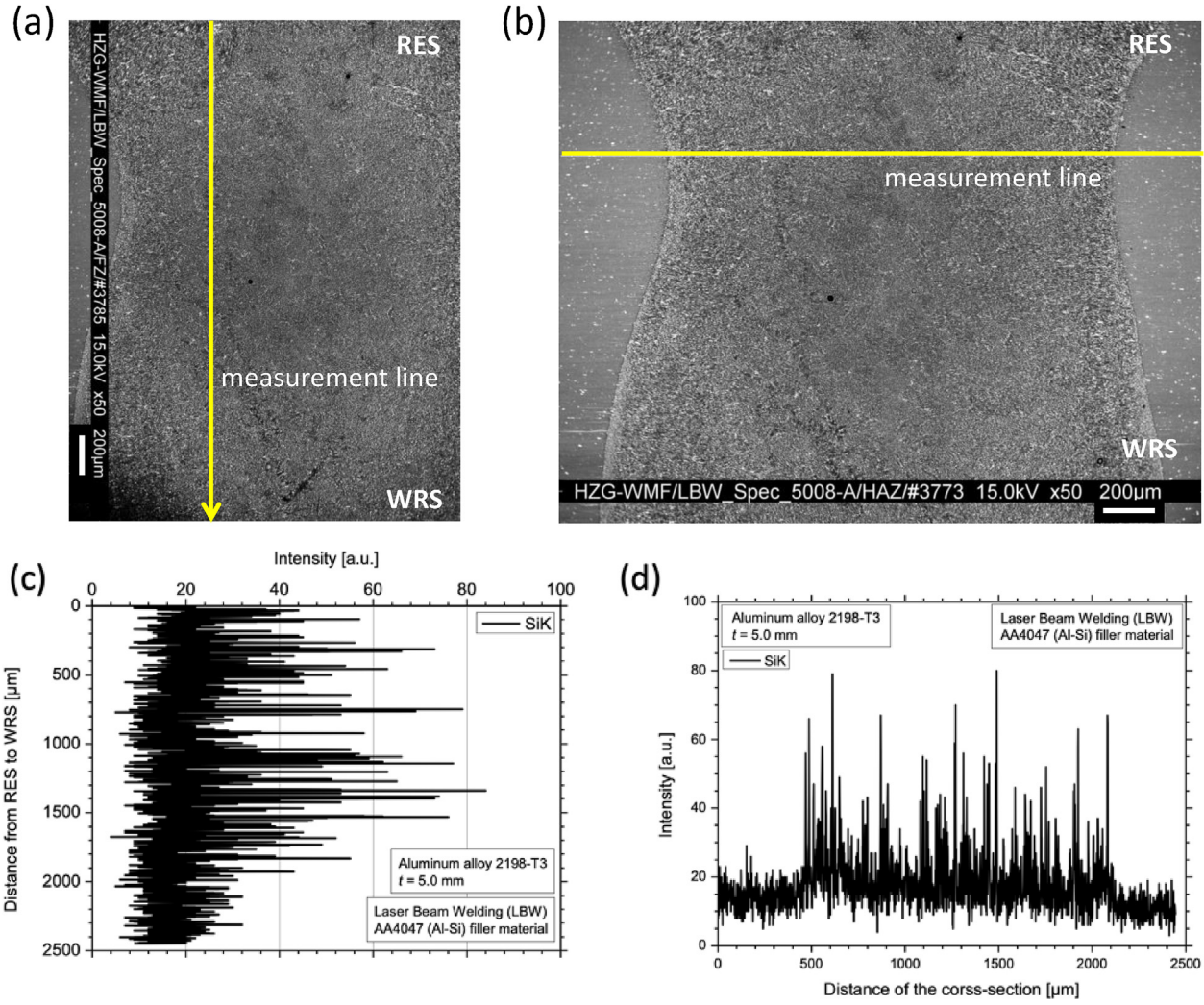

Fig. 4 – Locations of EDX measurement line (a) over the depth and (b) perpendicular to the welding direction with the respectively profiles of Si signal (c) in FZ and (d) in FZ/HAZ regions.

middle of the cross section, when compared with the top and bottom of the cross-section. The FZ presented average hardness values of around 87 $HV_{0.2}$, which is almost 20% lower than the respective hardness values within the HAZ.

3.3. *Local tensile mechanical properties*

Experimental stress–strain curves of both, horizontal and vertical MFT from the BM of Al–Li 2198-T3 alloy are presented in Fig. 6 Horizontal MFT specimens from the top (blue color curve) and bottom-line level (in red color line) of the cross-section presented similar ultimate tensile strength (R_m) values. The bottom-lime specimens exhibited slightly higher ductility A_T = 18.5% than the top-line specimens with A_T = 16.8%. The horizontal specimens from the middle line level of the cross-section presented the lowest tensile strength and ductility, when compared to the top and the bottom MFT specimens. The results agree with the mapping results of the hardness values of the welded joint in the previous section, which presented lower hardness values in the middle line of the cross-section, when compared with the top and bottom-line levels. To this end, the vertical specimens show similar tensile flow behavior with the horizontal specimens at the middle thickness (black vs green curve in Fig. 6a), but at a slightly higher stress level. However, this directional dependency is assumed be negligible for comparison purposes within this work.

Additionally, yield stress (R_p) results for all investigated horizontal and vertical specimens with the respective standard deviations under different artificial ageing times are summarized in Fig. 6b. BM specimens in T3 condition, exhibited R_p around 315 MPa for MFT specimens from the middle line level, while slightly higher results (approximately 330 MPa) can be seen for top and bottom line levels as well as for the vertical MFT specimens. With increasing ageing time up to 3 h, middle line level and vertical MFT specimens presented slightly lower R_p results (R_p = 402 MPa), in comparison with the top and bottom-line level horizontal specimens (R_p = 416 MPa). Yield stress increases with increasing ageing time up to 48 h for all MFT specimens regardless the extraction direction. For higher ageing time an essential decrease in R_p is

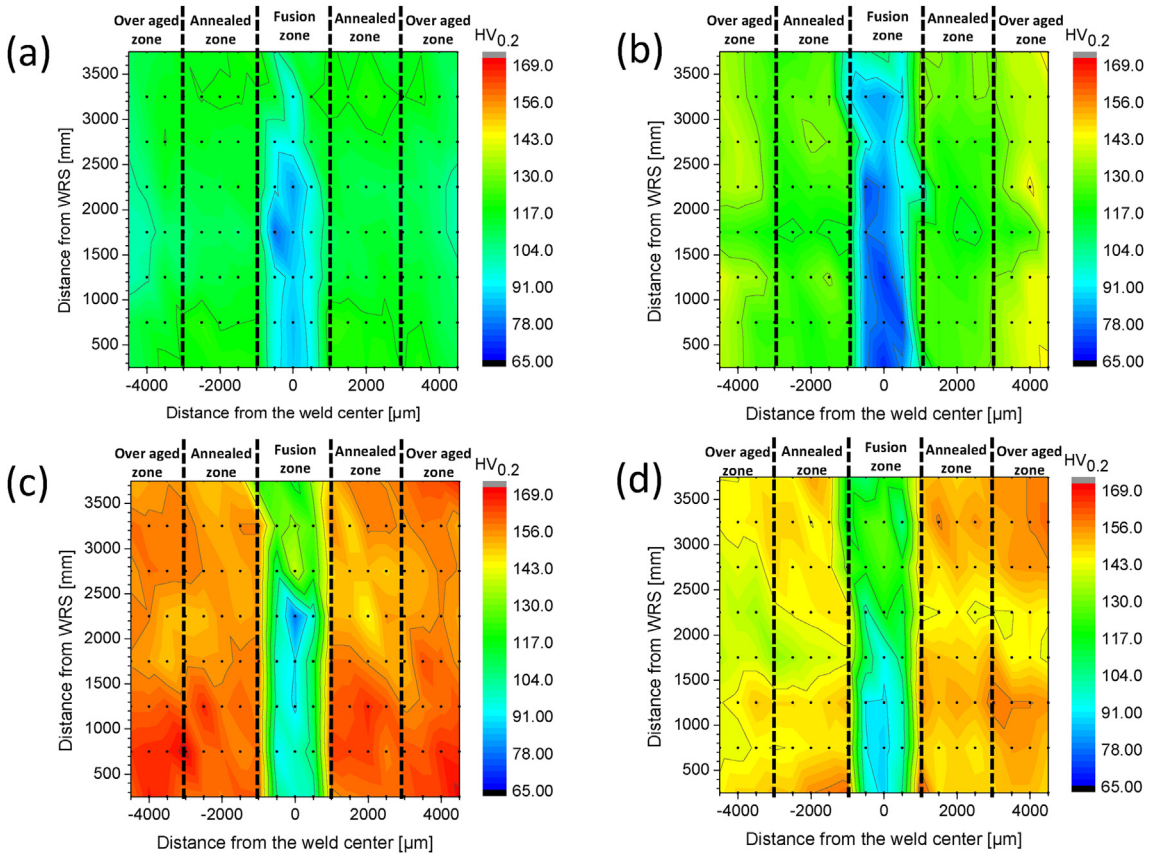

Fig. 5 – Hardness mapping of (a) as-welded (b) under-ageing (c) peak-ageing and (d) over-ageing condition of laser beam-welded AA2198-T3 joints.

noticed. These results agree well with corresponding results in the literature for the heat treatment of Al–Li alloys [9,36,37].

3.3.1. *Properties in the as-welded condition*

The nominal stress–strain tensile curves for the different zones with characteristic microstructures, which were obtained using MFT specimens of the as-welded AA2198 alloy with Al–Si filler material, are presented in Fig. 7. As it can be noticed, HAZ and FZ show distinctly different tensile mechanical behavior. As expected from the distribution of the hardness measurements, vertical MFT specimens from the HAZ show higher yield stress and ductility, when compared to the respective specimens from the FZ. MFT specimens from the FZ present a decrease in yield stress (~26%) and an increase in ductility from the RES to WRS. This yield stress decrease in the FZ can be explained by the non-uniform distribution of the filler wire material within the FZ.

3.3.2. *Effect of artificial ageing in local tensile mechanical properties*

The tensile test results of horizontal MFT specimens from different depth levels of the FZ and for various PWHT conditions are shown in Fig. 8. The obtained tensile test results from near the RES and for various ageing times are presented in Fig. 8a. As it can be noticed, with increasing artificial ageing time, there is a significant decrease in yield stress and ductility (total elongation at fracture A_T) at 3 h, when compared to the as-welded condition. With increasing ageing time up to 98 h, there is a continuous increase in yield stress; an increase in ductility is observed only after 48 h. For the MFT results from the middle of the weld in the FZ, similar trends are observed, Fig. 8b. It must be noted that at the middle of the weld, the Si content originating from the filler wire material is slightly lower when compared to the RES (approximately 0.2 wt.%). As can be seen in Fig. 8c for MFT specimens near the WRS within the FZ, there is a high increase in strength with increasing ageing time up to 98 h, while the ductility shows a similar trend as before. These differences in the local mechanical properties with increasing isothermal artificial ageing times can be correlated with the Si distribution in the FZ, see Fig. 4.

Vertical MFT specimens from the HAZ under different artificial ageing conditions are presented in Fig. 9. It can be seen that with increasing artificial ageing up to 48 h there is a continuous increase in yield stress up to 500 MPa with a simultaneous decrease in ductility. For 98 h artificial ageing there is a slight decrease in yield stress with a slight increase in ductility when compared with the respective results for 48 h. The HAZ, which is located beside the FZ, is a non-welded area, which is affected by the momentarily heat during the welding process. Nevertheless, this heat leads to grain growth within this zone and for that reason, the tensile mechanical behavior within the HAZ is slightly different from the respective results of the BM with increasing ageing time for 170 °C [30].

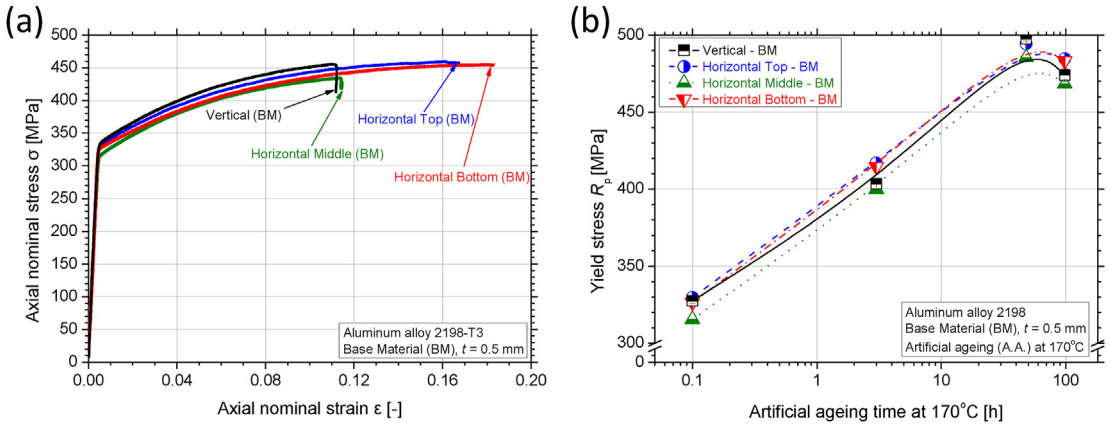

Fig. 6 – (a) Stress–strain curves of BM AA2198-T3 alloy for vertical and horizontal micro-flat tensile specimens; (b) Yield stress (R_p) values of vertical and horizontal micro-flat tensile specimens from the BM AA2198 alloy under different PWHT conditions.[11]

Fig. 10 summarizes the yield stress and the total elongation at fracture results of horizontal and vertical MFT specimens, respectively, under different artificial ageing conditions. Vertical MFT specimens from the HAZ show a continuous increase in yield stress up to 98 h/170 °C (~70%), Fig. 10a. In comparison, horizontal MFT specimens from the FZ and in the as-welded condition, present a decrease by about 40% in yield stress. Specimens from near the RES show an increase in yield stress by approximately 46%, with increasing artificial ageing from 3 h up to 98 h/170 °C. Yield stress results are slightly higher for the specimens from the middle-line level of the cross-section when compared with the respective MFT specimens from the RES. With increasing ageing time up to 98 h/170 °C, there is a continuous increase in yield stress by about 52%. MFT specimens from near the WRS presented an opposite trend, with a continuous increase of yield stress up to 48 h/170 °C and PA condition.

The total elongation at fracture results of the investigated MFT specimens under different artificial ageing heat treatment conditions can be seen in Fig. 10b. It can be noticed that an essential increase of the yield stress is simultaneously followed by a decrease in tensile ductility. To this end, MFT specimens from the HAZ show a high decrease in ductility from 13% to 5.7% with increasing ageing times. On the other hand, MFT specimens from the FZ presented a decrease in ductility, which always attains minimum values of approximately 1.5% elongation. In comparison, vertical specimens from the HAZ presented a higher decrease in ductility compared with the horizontal MFT specimens of approximately 6% and 2.5% respectively.

3.4. *Proposed approximations*

In the present investigation, two approximations between hardness measurements and tensile mechanical properties are proposed. These approximations might be used to facilitate the acquisition of the necessary mechanical properties for a fast calculation of the mechanical behaviour of the welded joints and therefore suitable to reduce the time and effort to manufacture the testing specimens. According to Tiryakioğlu et al. [38] the relation between hardness and tensile properties for strain-hardening materials like Al, Cu, and Mg alloys can be written in the form

$$\sigma = \beta_0 + \beta_1 HV \quad (1)$$

where β_0 and β_1 are y-intercept and slope in the proposed σ-HV diagram, respectively. Eq. (1) will be used in the present study in the form that is proposed by Tiryakioğlu et al. in [38,39] for age-hardenable alloys, to address the findings in the heat-treatment conditions of AA2198.

Based on the experimental results of LBWed AA2198, Fig. 11 illustrates the correlation between yield stress and strain hardening exponent to hardness data of the present study and comprised the combinations of different heat treatment conditions and specimen locations. The linear regression analysis of the yield stress, Fig. 11a, leads to $R^2 = 0.771$. The proposed approximation between yield stress R_p, in MPa, and Vickers hardness HV is expressed as:

$$R_p = -218.49 + 4.45\,HV \quad (2)$$

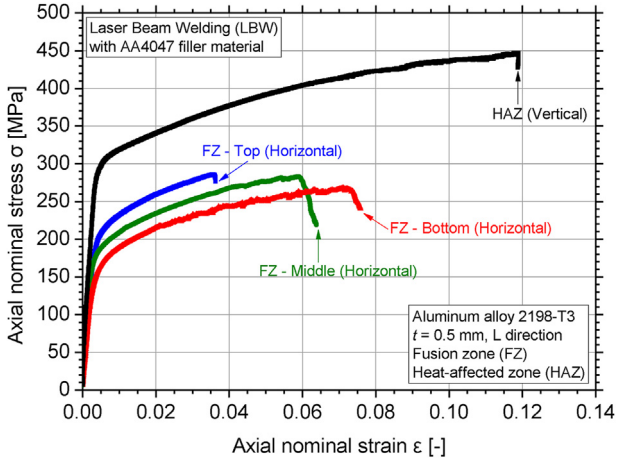

Fig. 7 – Typical tensile flow curves of vertical and horizontal micro-flat tensile specimens from heat-affected and fusion zone, respectively, of laser beam welded aluminum-lithium alloy AA2198-T3 joints in as-welded condition.

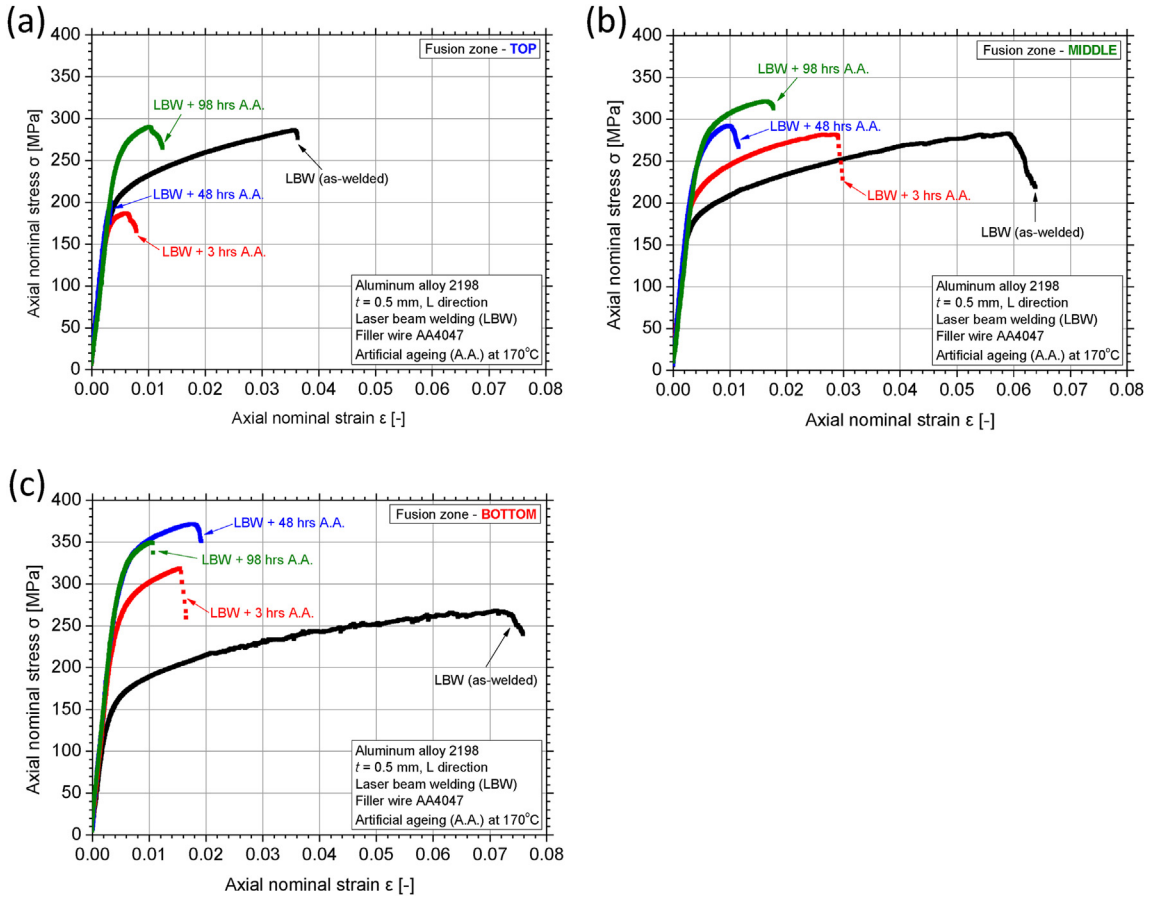

Fig. 8 – Typical tensile flow curves of horizontal micro-flat tensile specimens from (a) top, (b) middle and (c) bottom positions of FZ of laser beam-welded aluminum-lithium alloy AA2198-T3 joints for different PWHT conditions.

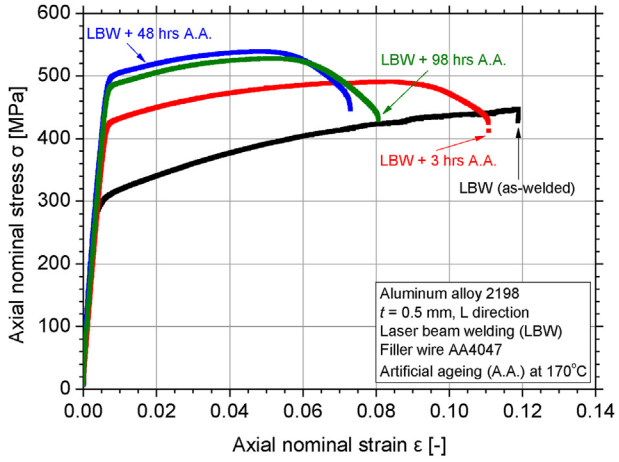

Fig. 9 – Typical tensile flow curves of vertical micro-flat tensile specimens from HAZ of laser beam-welded AA2198-T3 joints for different PWHT conditions.

To model and analyze the tensile flow behavior of the welded joint, a constitutive equation must be employed for the fast approximation of the tensile mechanical behavior of each different regions of the welded joint. We propose a simplistic constitutive law $\sigma = R_p + K\varepsilon_p^n$, where K is the strength coefficient, ε_p is the plastic strain, and n is the strain hardening exponent. In this work, a correlation between strain hardening exponent and hardness is proposed, see Fig. 11b. Similar to the previous approximation, linear regression is assumed and despite its simplistic nature, it can be exploited for the specific alloy and its heat treatments, as derived from the extensive experimental database of the present investigation. The analysis shows the best linear fit with correlation coefficient R-Square of 0.824, leading to:

$$n = 0.308 - 0.00175\,HV \tag{3}$$

Fig. 12a shows the resulting approximations (in symbols) for the three different positions over the depth of FZ of the AA2198 alloy. The respective experimental test curves (in solid lines) are presented as well. As it can be seen, the approximated results fit very well with the experimental results. The yield stress results show a deviation of ~9% at maximum, where a slightly higher decrease can be noticed for the UTS.

The resulting approximation of the stress–strain behavior and the respective experimental results for the HAZ under different artificial ageing conditions are illustrated in Fig. 12b. In the T3 condition, the yield stress is almost similar for both

[1] Please note that the results were appointed to a small ageing time of 0.1 h, to allow illustration in logarithmic scale.

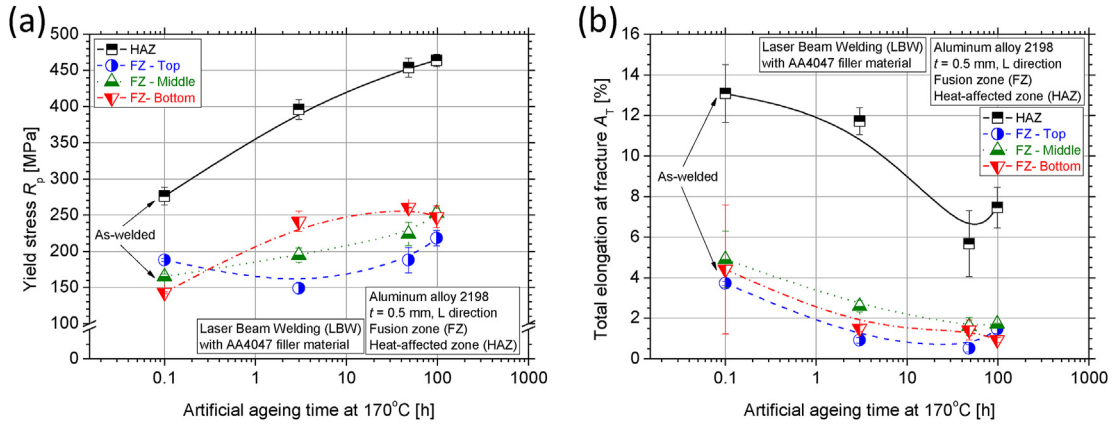

Fig. 10 – (a) Yield stress R_p and (b) total elongation at fracture A_T values of horizontal and vertical micro-flat tensile specimens from different regions of laser beam-welded AA2198-T3 joints for different PWHT conditions.[21]

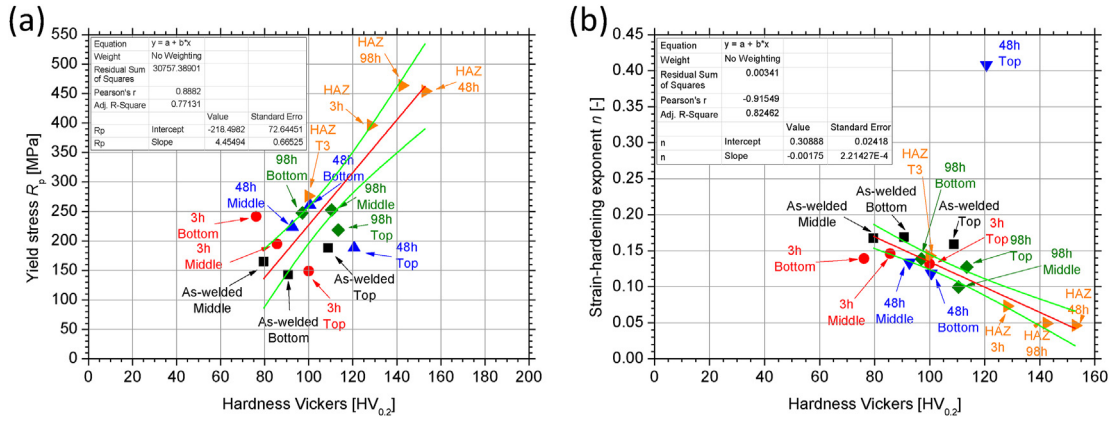

Fig. 11 – Approximations between (a) hardness measurements and yield stress and (b) hardness measurements and strain-hardening exponent values.

cases, while the UTS shows a deviation of about 9%. With increasing ageing time up to 3 h, a slight deviation can be noticed between the proposed approximation and the experimental data. For an additional increase of ageing holding time up to 48 h and PA condition, yield stress shows a maximum deviation of about 6%. In summary, the proposed approximation provides a good fit of the experimental results for the different ageing conditions.

The observed deviations are mainly related due to the local variation and the present experimental scatter in the HV measurements. However, the comparisons show that the proposed approximation can be exploited for a fast prediction of the local tensile flow stress–strain curves of AA2198 joints.

4. Finite element modeling

4.1. *Model set-up*

A detailed three dimensional parametric finite element model of the weld was developed to evaluate the effect of weld geometry and geometrical imperfections on the developed stress and strain fields in the welded joint under axial loading. The local tensile mechanical properties, which were obtained in the previous section for LBWed AA2198 alloy, were used as an input to the model. The geometry of the gauge length of a tensile specimen was modelled using the commercial finite element software ANSYS, conducting elasto-plastic analyses, Fig. 13. Due to the symmetry of the problem, only a quarter of the specimen was modelled, and appropriate symmetry boundary conditions were used, Fig. 13a. An incremental axial displacement was applied to the free end up to a maximum nominal strain of 1.5% [30]. Convergence tests regarding the mesh size were conducted, where the converged model consisted of approximately 23.000 elements with element size close to 0.2 mm in the FZ. Fig. 13b shows that the gauge length (50 mm) of the tensile test specimen was divided into three regions: BM, HAZ, and FZ. Furthermore, FZ was divided into three more regions to insert the local mechanical properties from the MFT at the three different depth levels. The mechanical properties for the BM were taken from the previous works of the authors [30,40].

The geometrical imperfections, investigated in the present work, are illustrated in Fig. 14. The width and the angle

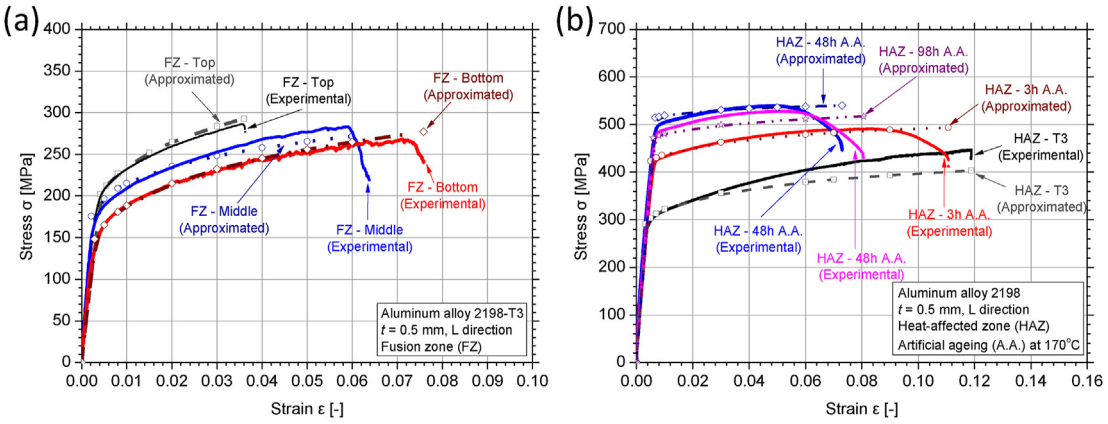

Fig. 12 – Comparison between experimental and approximated stress–strain curves for (a) fusion zone in the as-welded condition and (b) heat-affected zone under different artificial ageing conditions.

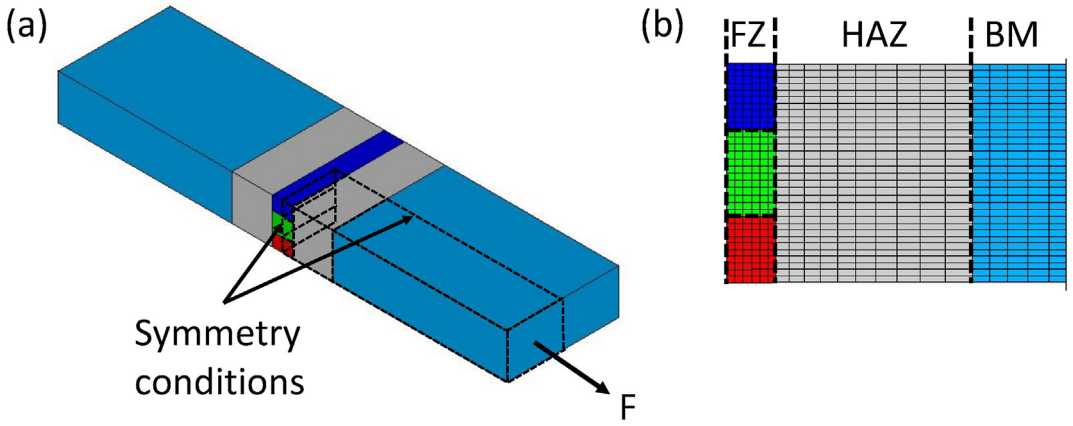

Fig. 13 – (a) Finite element model and (b) detailed view of different modelled zones. The different colors in the fusion zone refer to the different volumes with different local mechanical properties.

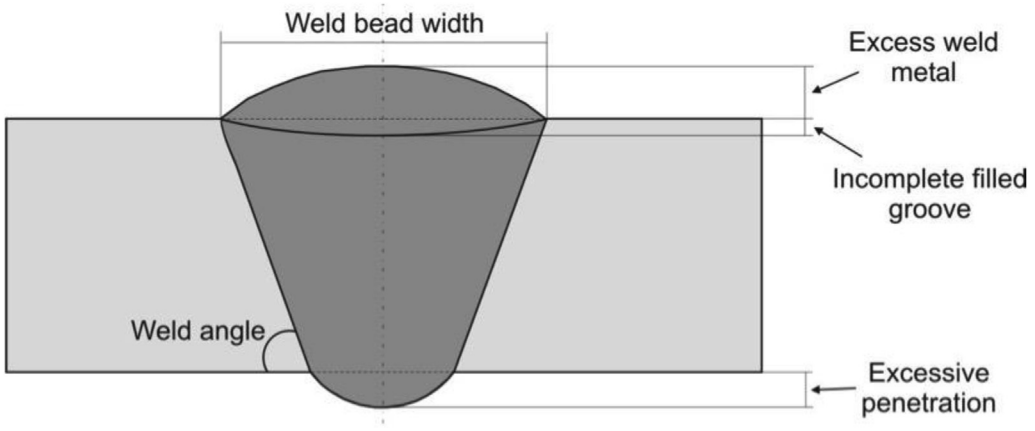

Fig. 14 – Geometrical imperfections considered during the FE analyses.

of the weld were varied from 1.75 to 2.75 mm and 90 to 80°, respectively, [41]. According to ISO 13919–2 [42], excess weld metal, excessive penetration, and incompletely filled groove are permitted according to quality *B* level. For the excess weld metal and excessive penetration according to *B* level, they should comply to $h \leq 0.2 + 0.15\,t$ (where h is the size of the imperfection – height or width - and t is the thickness of the specimen), with a maximum of 5 mm. Similar for the incomplete filled groove, *B* level requires $h \leq 0.05$, with a maximum of 1 mm. For that reason, the parameters used in

[2] Please note that the results were appointed to a small ageing time of 0.1 h, to allow illustration in logarithmic scale.

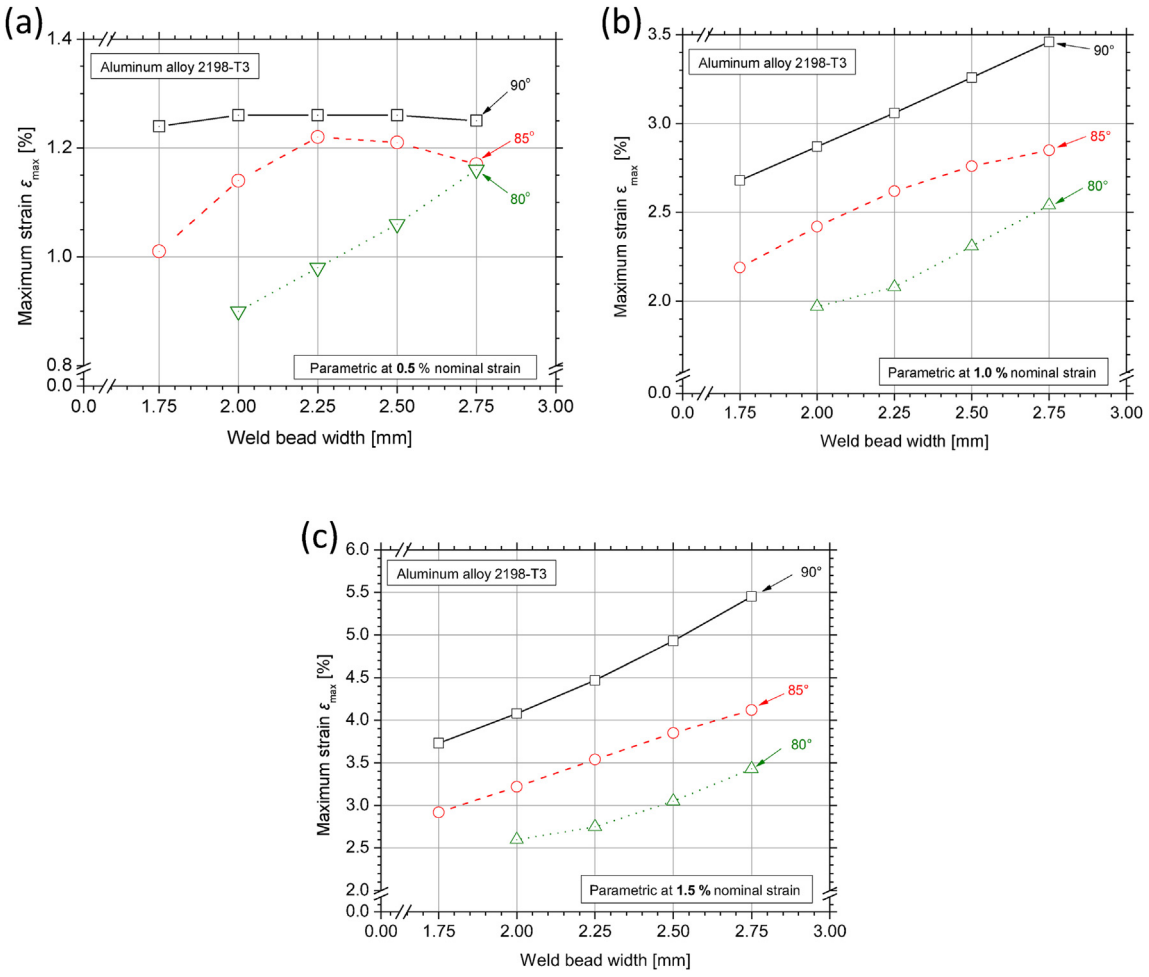

Fig. 15 – Relation between maximum stain ε_{max} and weld bead width for different parametric nominal strain (a) 0.5%, (b) 1.0% and (c) 1.5% in the as-welded condition and for different weld angles (90°, 85°, 80°).

the present study were the excessive penetration and excess weld metal ranging from 0.3 mm to 0.9 mm, while the incompletely filled groove ranged from 0.05 mm to 0.25 mm.

4.2. *Numerical results*

The results of the analyses are presented in terms of the maximum equivalent strain, which was observed in the FZ or at the boundary between FZ and HAZ. The relation between the maximum equivalent strain developed in the model and weld bead width for the as-welded condition is presented in Fig. 15. For higher nominal strains of 1% and 1.5%, the maximum strain varies almost linear with the weld bead width. Close examination of the strain distribution indicates that there is re-distribution of the local strain between the different areas at low nominal strain, and that the position of maximum strain changes depending on the weld angle. In all cases examined, a higher weld angle corresponds to higher maximum strain at the FZ. This can be attributed to the reduction of weld bead width at the lower side for lower angles.

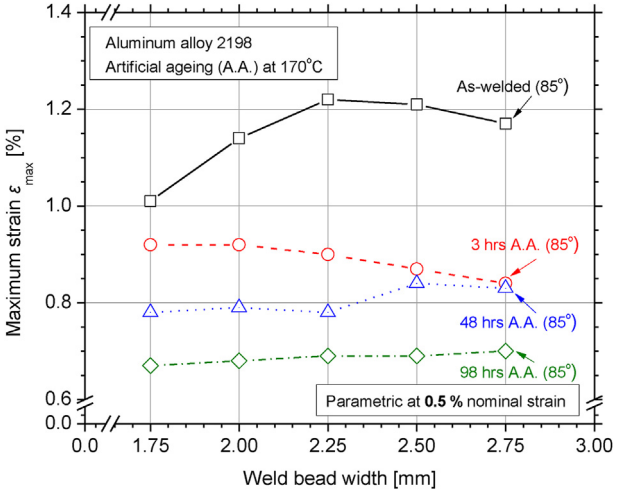

Fig. 16 – Relation between maximum stain ε_{max} and weld bead width at 0.5% nominal strain for AA2198 under different artificial ageing conditions.

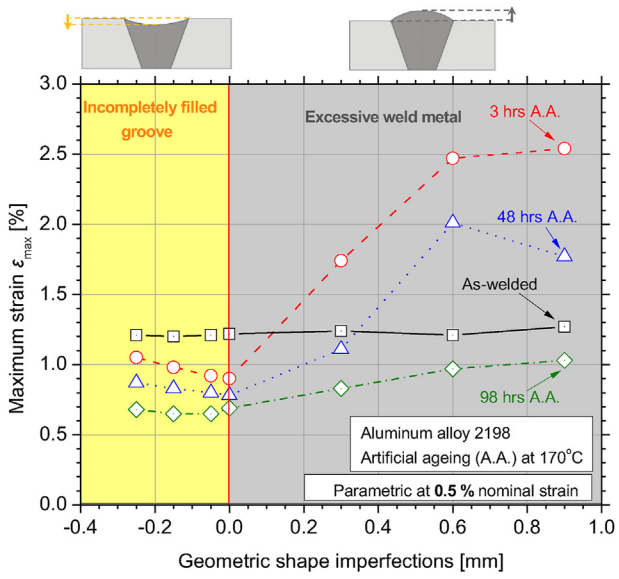

Fig. 17 – Relation between maximum stain ε_{max} and geometric shape imperfections at 0.5% nominal strain for AA2198 under different artificial ageing conditions.

Fig. 16 shows the strain evolution as predicted by the model for AA2198 under different artificial ageing conditions for an applied strain of 0.5%. Maximum strain decreases with increase of artificial ageing up to 98 h/170 °C when compared with the as-welded condition. With increasing artificial ageing time up to 3 h/170 °C, there is a continuous decrease of the maximum strain of about 9% from 1.75 mm up to 2.75 mm weld bead width. A further decrease is observed by applying ageing time up to 48 h/170 °C. A plateau is achieved for lower weld bead width, while from 2.25 mm up to 2.75 mm there is an increase in maximum strain by approximately 10%. For longer ageing periods (>48 h/170 °C) a slight increase of maximum strain of about 11% can be noticed with increasing weld bead width. The above results for 3 and 48 h/170 °C can be attributed to strain localization due to lower yield stress at the top region of the weld, see Fig. 8a.

The effect of geometrical imperfections of an incompletely filled groove and excessive weld metal under different artificial ageing conditions are presented in Fig. 17. For comparison purposes, the average weld bead width (2.25 mm) and angle (85°) were kept fixed. It can be observed that for the as-welded condition no significant change occurred for both imperfections. The incompletely filled groove leads to a decrease in maximum strain with increasing ageing time up to 98 h/170 °C, while no significant change can be noticed by decreasing the geometric shape imperfection from 0.25 to 0.05 mm. An opposite trend can be seen for the excessive weld metal with a continuous increase of maximum strain for 3 h/170 °C with increasing the excessive weld metal imperfection from 0 up to 0.6 mm. Similar trends can be observed for the other ageing conditions as well.

Fig. 18 shows a typical strain distribution as predicted by the model, to demonstrate the position of the maximum strain. The distribution along the width in the middle of the FZ, which was further subdivided into three different height levels, according to the experimental extraction positions of the MFT specimens, is illustrated in Fig. 18b. Fig. 19 displays the variation of the position of maximum strain for different weld angles at a specific weld bead width of 2.25 mm. Specifically, for the applied strain of 1.0%, the position of the

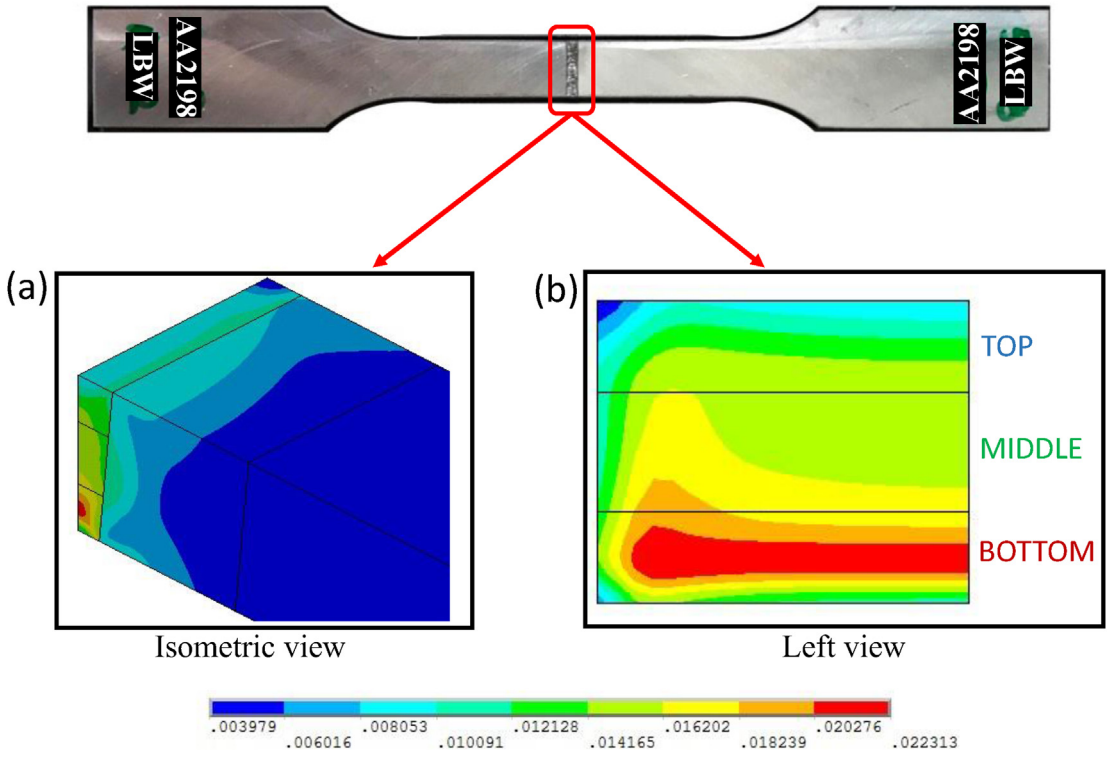

Fig. 18 – Typical strain distributions (a) within the gauge section of the tensile specimen (only quarter is shown) and (b) within fusion zone, which is subdivided into three regions according to the MFT specimens.

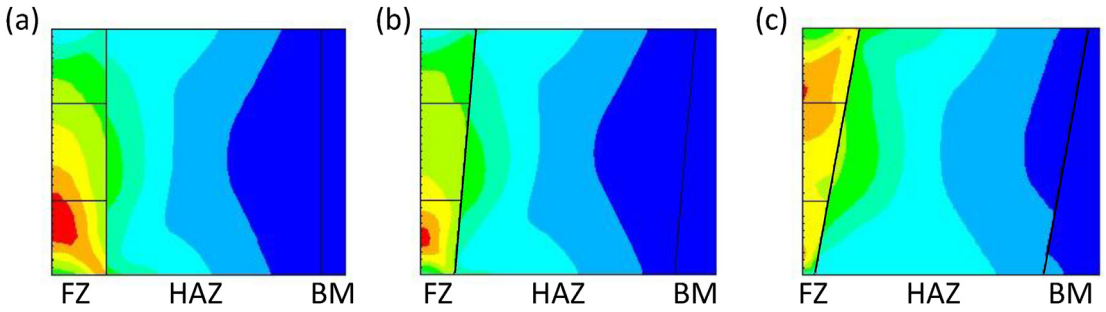

Fig. 19 – Position of maximum strain (indicated by the red color) for 1.0% nominal strain, for different weld angles (a) 90°, (b) 85° and (c) 80° at a weld width of 2.25 mm.

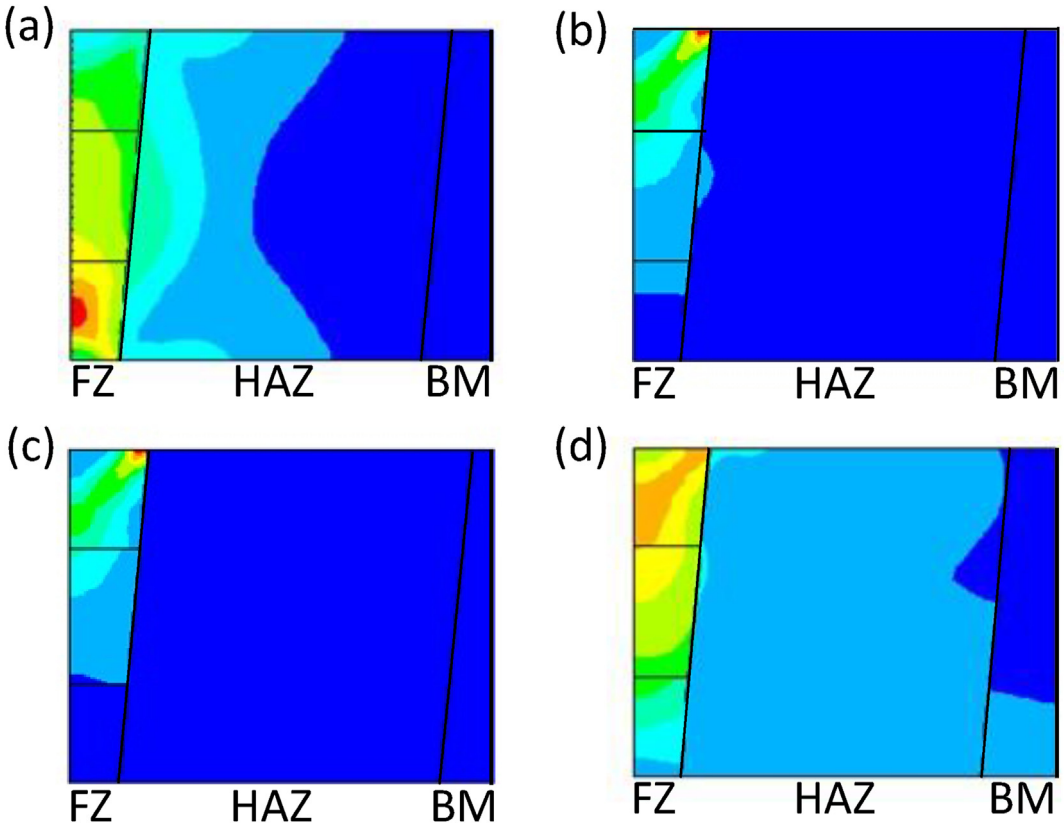

Fig. 20 – Position of maximum strain (indicated by the red color) for AA2198 under different artificial ageing conditions; (a) as-welded, (b) 3 h, (c) 48 h and (d) 98 h, for 0.5% nominal strain, with weld bead width of 2.25 mm and weld angle of 85°.

maximum strain can be observed in the lower region of the FZ for the higher weld angles of 90° and 85°, while for the lower weld angle of 80° the position of the maximum strain is located between the upper and middle region of the FZ. These differences can be attributed to the change of the lower weld bead width, which decreases due to the respective decrease of the weld angle to 80°.

The effect of PWHT is presented in Fig. 20. With increasing artificial ageing to 98 h the position of the maximum strain changes from the lower to the upper region of the FZ. This explains the significant effect of excessive weld metal on maximum strain as presented in Fig. 17. To this end, it has to be mentioned that the position and value of maximum strain provides only an indication of the qualitative effects of geometry and shape imperfections on the joint performance. But the results indicate potential weak points of the joint and provides a first qualitative comparison of the performance of the joint strength based on the different geometric features.

5. Conclusions

The findings of the present investigation are summarized as follows:

1) Microstructural analysis of the as-welded AA2198 alloy shows that EQZ and PMZ are evident within the TZ. The EQZ in the present study was found to be narrow, when

compared to other Al–Li alloys according to the literature, due to the different chemical composition of the filler material that affects the width of the zone.

2) The filler material addition in the welded joint increased the Si concentration within the FZ, when compared to the HAZ. However, in the depth of the FZ, from the RES to the WRS, the Si content decreases.
3) A gradient on the local mechanical properties of the AA2198 alloy in the as-welded condition was noticed; a decrease in yield stress in the FZ by approximately 26% was followed by a respectively increase in tensile ductility from the RES to the WRS.
4) Different local mechanical properties over the depth of the FZ by applying PWHT were observed. Higher yield stress values were noticed for the bottom-line level by approximately 52% with an increase of ageing time up to 48 h/170 °C and PA condition. However, all investigated specimens showed a decrease in tensile ductility with increasing ageing times.
5) Two different linear approximations, based on the performed mechanical tests, were proposed to facilitate the evaluation of the local mechanical properties of the welded joints.
6) The FE results show that the maximum strain occurs in the lower region of the FZ for weld angles of 90° and 85°. In contrast, for the lower weld angle of 80° the position of the maximum strain was observed between the upper and the middle region of the FZ, which can be attributed to the change of the weld bead width that is smaller in the lower region due to the respective effect of the weld angle.
7) Using the experimental results for the specimens under different PWHT within the FE model, maximum strain appears in the upper region for all investigated ageing times. With increasing ageing holding time up to PA condition, there is an obvious strain concentration in the upper region and especially between the FZ and HAZ.

Declaration of Competing Interest

The authors declare that they have no known competing financial interests or personal relationships that could have appeared to influence the work reported in this paper.

Acknowledgments

The authors would like to thank Dr. V. Ventzke for performing EDX analysis and Mr. M. Horstmann and Mr. H. Tek from the Department of Laser Processing and Structural Assessment of Helmholtz Zentrum Hereon for their valuable technical support. This publication was funded by the Open Access Publication Fund of the Leuphana University Lüneburg, which is gratefully acknowledged.

REFERENCES

[1] Montgomery J. Aircraft primary structure and materials" national institute of aerospace workshop. Hampton, VA: Revolutionary Aircraft for Quite Communities; 2007.
[2] Rioja RJ, Liu J. The evolution of Al–Li base products for aerospace and space applications. Metall Mater Trans 2012;43:3325–37. https://doi.org/10.1007/s11661-012-1155-z.
[3] Prasad NE, Gokhale AA, Rao PR. Mechanical behaviour of aluminium-lithium alloys. Sadhana 2003;28:209–46. https://doi.org/10.1007/BF02717134.
[4] Lavernia EJ, Grant NJ. Aluminium-lithium alloys. J Mater Sci 1987;122:1521–9. https://doi.org/10.1007/BF01132370.
[5] Dursun T, Soutis C. Recent developments in advanced aircraft aluminum alloys. Mater Des 2014;56:862–71. https://doi.org/10.1016/j.matdes.2013.12.002.
[6] Yoshimura R, Konno TJ, Abe E, Hiraga K. Transmission electron microscopy study of the evolution of precipitates in aged Al–Li–Cu alloys: the h' and T1 phases. Acta Mater 2003;51:4251–66. https://doi.org/10.1016/S1359-6454(03)00253-2.
[7] Decreus B, Deschamps A, De Geuser F, Donnadieu P, Sigli C, Weyland M. The influence of Cu/Li ratio on precipitation in Al–Cu–Li–x alloys. Acta Mater 2013;61:2207–18. https://doi.org/10.1016/j.actamat.2012.12.041.
[8] Jo HH, Hirano KI. Precipitation process in Al-Cu-Li alloy studied by DSC. Mater Sci Forum 1987;13–14:377–82. https://doi.org/10.4028/www.scientific.net/MSF.13-14.377.
[9] Alexopoulos ND, Proiou A, Examilioti TN, Kashaev N, Riekehr S, Kourkoulis SK. Mechanical performance of (Al-Cu) 2024 and (Al-Cu-Li) 2198 aluminum alloys under different artificial ageing conditions. Procedia Struct Integr 2016;2:3782–3. https://doi.org/10.1016/j.prostr.2016.06.077.
[10] Zhang SF, Zeng WD, Yang WH, Shi CL, Wang HJ. Ageing response of a Al-Cu-Li 2198 alloy. Mater Des 2014;63:368–74. https://doi.org/10.1016/j.matdes.2014.04.063.
[11] Tao J, Zhang L, Wo G, Chen A, Zhang X, Shi C. Effect of heat treatment on the microstructure and mechanical properties of extruded Al–4Cu–1Li–0.4Mg–0.4Ag–0.18Zr Alloy. Mater Sci Eng A 2018;717:11–9. https://doi.org/10.1016/j.msea.2018.01.063.
[12] Pacchione M, Telgkamp J. Challenges of the metallic fuselage. In: Proc. 25th international congress of the aeronautical sciences. Hamburg: International Council of the Aeronautical Sciences (ICAS); 2006.
[13] Gialos AA, Zeimpekis V, Alexopoulos ND, Kashaev N, Riekehr S, Karanika A. Investigating the impact of sustainability in the production of aeronautical subscale components. J Clean Prod 2018;176:785–99. https://doi.org/10.1016/j.jclepro.2017.12.151.
[14] Enz J, Riekehr S, Ventzke V, Kashaev N. Influence of the local chemical composition on the mechanical properties of laser beam welded Al-Li alloys. Phys Procedia 2012;39:51–8. https://doi.org/10.1016/j.phpro.2012.10.013.
[15] Ning J, Zhang L, Bai Q, Yin X, Niu J, Zhang J. Comparison of the microstructure and mechanical performance of 2A97 Al-Li alloy joints between autogenous and non-autogenous laser welding. Mater Des 2017;120:144–56. https://doi.org/10.1016/j.matdes.2017.02.003.
[16] Zhang X, Huang T, Yang W, Xiao R, Liu Z, Li L. Microstructure and mechanical properties of laser beam-welded AA2060 Al-Li alloy. J Mater Process Technol 2016;237:301–8. https://doi.org/10.1016/j.jmatprotec.2016.06.021.
[17] Zhang X, Yang W, Xiao R. Microstructure and mechanical properties of laser beam welded Al-Li alloy 2060 with Al-Mg filler wire. Mater Des 2015;88:446–50. https://doi.org/10.1016/j.matdes.2015.08.144.
[18] Lippold JC, Lin W. Weldability of commercial Al-Cu-Li alloys. Mater Sci Forum 1996;217–222:1685–90. https://doi.org/10.4028/www.scientific.net/MSF.217-222.1685.
[19] Kostrivas T, Lippold JC. Weldability of Li-bearing aluminum alloys. Int Mater Rev 1999;44:217–37. https://doi.org/10.1179/095066099101528289.

[20] Nayan N, Yadava M, Sarkar R, Murty SVSN, Gurao NP, Mahesh S, et al. Microstructure and tensile response of friction stir welded Al-Cu-Li (AA2198-T8) alloy. Mater Char 2020;159:110002. https://doi.org/10.1016/j.matchar.2019.110002.
[21] Wang FF, Li WY, Shen J, Zhang ZH, Li JL, dos Santos JF. Global and local mechanical properties and microstructure of Bobbin tool friction-stir-welded Al–Li alloy. Sci Technol Weld Join 2016;21:479–83. https://doi.org/10.1080/13621718.2015.1132128.
[22] Uematsu Y, Kakiuchi T, Niimi K, Toasa Caiza PD. Local strain analysis under quasi-static tensile loading in Al/steel dissimilar friction stir weld by a digital image correlation method. Int J Adv Manuf Technol 2022;120:349–60. https://doi.org/10.1007/s00170-021-08481-6.
[23] Rao D, Heerens J, Alves Pinheiro G, dos Santos JF, Huber N. On characterisation of local stress-strain properties in friction stir welded aluminium AA 5083 sheets using micro-tensile specimen testing and instrumented indentation technique. Mater Sci Eng A 2010;527:5018–25. https://doi.org/10.1016/j.msea.2010.04.047.
[24] Ambriz RR, Chicot D, Benseddiq N, Mesmacque G, de la Torre SD. Local mechanical properties of the 6061-T6 aluminium weld using micro-traction and instrumented indentation. Eur J Mech A/Solids 2011;30:307–15. https://doi.org/10.1016/j.euromechsol.2010.12.007.
[25] Ma Y, Takikawa A, Nakanishi J, Doira K, Shimizu T, Lu Y, et al. Measurement of local material properties and failure analysis of resistance spot welds of advanced high-strength steel sheets. Mater Des 2021;201:109505. https://doi.org/10.1016/j.matdes.2021.109505.
[26] Ma Y, Yu Y, Geng P, Ihara R, Maeda K, Suzuki R, et al. Fracture modeling of resistance spot welded ultra-high-strength steel considering the effect of liquid metal embrittlement crack. Mater Des 2021;210:110075. https://doi.org/10.1016/j.matdes.2021.110075.
[27] Dhondt M, Aubert I, Saintier N, Olive JM. Mechanical behavior of periodical microstructure induced by friction stir welding on Al-Cu-Li 2050 alloy. Mater Sci Eng A 2015;644:69–75. https://doi.org/10.1016/j.msea.2015.05.072.
[28] Rao D, Huber K, Heerens J, dos Santos JF, Huber N. Asymmetric mechanical properties and tensile behaviour prediction of aluminium alloy 5083 friction stir welding joints. Mater Sci Eng A 2013;565:44–50. https://doi.org/10.1016/j.msea.2012.12.014.
[29] Puydt Q, Flouriot S, Ringeval S, De Geuser F, Estevez R, Parry G, et al. Relationship between microstructure, strength, and fracture in an Al-Zn-Mg electron beam weld: Part II: mechanical characterization and modeling. Metall Mater Trans 2014;45:6141–52. https://doi.org/10.1007/s11661-014-2567-8.
[30] Examilioti TN, Kashaev N, Ventzke V, Klusemann B, Alexopoulos ND. Effect of filler wire and post weld heat treatment on the mechanical properties of laser beam-welded AA2198. Mater Charact 2021;178:111257. https://doi.org/10.1016/j.matchar.2021.111257.
[31] ISO 6507-1, Metallic materials — Vickers hardness test — Part vol. 1: Test method; 2005.
[32] Gutierrez A, Lippold JC. A proposed mechanism for equiaxed grain formation along the fusion boundary in aluminum-copper-lithium alloys. Weld J 1998;77:123–32.
[33] Lin DC, Wang GX, Srivatsan TS. A mechanism for the formation of equiaxed grains in welds of aluminum-lithium alloy 2090. Mater Sci Eng A 2003;351:304–9. https://doi.org/10.1016/S0921-5093(02)00858-4.
[34] Fu B, Qin G, Meng X, Ji Y, Zou Y, Lei Z. Microstructure and mechanical properties of newly developed aluminum–lithium alloy 2A97 welded by fiber laser. Mater Sci Eng A 2014;617:1–11. https://doi.org/10.1016/j.msea.2014.08.038.
[35] Kashaev N, Chupakhin S, Enz J, Ventzke V, Groth A, Horstmann M, et al. Fatigue and fatigue crack propagation of laser beam-welded AA2198 joints and integral structures. Adv Mat Res 2014;891–892:1457–62. https://doi.org/10.4028/www.scientific.net/AMR.891-892.1457.
[36] Chen X, Ma X, Xi H, Zhao G, Wang Y, Xu X. Effects of heat treatment on the microstructure and mechanical properties of extruded 2196 Al-Cu-Li alloy. Mater Des 2020;192:108746. https://doi.org/10.1016/j.matdes.2020.108746.
[37] Cui S, Zhang C, Liu M, Chen L, Zhao G. Precipitation behavior of an Al–Cu–Li–X alloy and competing relationships among precipitates at different aging temperatures. Mater Sci Eng A 2021;814:141125. https://doi.org/10.1016/j.msea.2021.141125.
[38] Tiryakioğlu M, Robinson JS, Salazar-Guapuriche MA, Zhao YY, Eason PD. Hardness–strength relationships in the aluminum alloy 7010. Mater Sci Eng A 2015;631:196–200. https://doi.org/10.1016/j.msea.2015.02.049.
[39] Tiryakioğlu M, Robinson JS. On the representative strain in Vickers hardness testing of 7010 aluminum alloy. Mater Sci Eng A 2015;641:231–6. https://doi.org/10.1016/j.msea.2015.06.038.
[40] Examilioti TN, Klusemann B, Kashaev N, Riekehr S, Enz J, Alexopoulos ND. Anisotropy and size effect in tensile mechanical properties of Al-Cu-Li 2198 alloy. Procedia Struct Integr 2017;5:13–8. https://doi.org/10.1016/j.prostr.2017.07.052.
[41] Examilioti TN, Kashaev N, Enz J, Klusemann B, Alexopoulos ND. On the influence of laser beam welding parameters for autogenous AA2198 welded joints. Int J Adv Manuf 2020;110:2079–92. https://doi.org/10.1007/s00170-020-05893-8.
[42] ISO 13919-2. Welding—electron and laser-beam welded joints—guidance on quality levels for imperfections—Part 2: aluminium and its weldable alloys. Geneva, Switzerland: International Organization for Standardization; 2001.